J Ther Eng, Vol. 12, No. 1, pp. 88−98, January, 2026

Journal of Thermal Engineering
Web page info: https://jten.yildiz.edu.tr
DOI: 10.14744/thermal.0001060

Research Article

Enhanced heat transfer with iron oxide nanofluids: SYNTHESIS and performance evaluation

Mehdi AMIRI[1,*], Rasoul KARIMI[2], Iman ABBASPOUR[2]

[1]*Department of Physics, Faculty of Sciences, University of Mohaghegh Ardabili, Ardabil, 56131, Iran*
[2]*Faculty of Mechanical Engineering, University of Imam Khomeini Marine Sciences, Nowshahr, 46516, Iran*

ARTICLE INFO

Article history
Received: 14 October 2024
Accepted: 18 May 2025

Keywords:
Co-precipitation Method; Critical Heat Flux (CHF); Heat Exchangers; Heat Transfer Enhancement; Iron(II, III) Oxide; Magnetic Nanoparticles; Nanofluids

ABSTRACT

The low thermal conductivity of conventional fluids like water poses a significant challenge in heat transfer applications. In this study, iron oxide (Fe_3O_4) nanoparticles were synthesized using the co-precipitation method with precise size control. Two samples were prepared by adjusting the pH with NH_4OH (Sample 1: 29.42 nm) and NaOH (Sample 2: 38.04 nm). Characterization using XRD, SEM, and TEM confirmed cubic-phase Fe_3O_4 with spherical morphology. Stable nanofluids were prepared using Arabic gum as a stabilizing agent, achieving zeta potential values of -31.7 and -35.2 mV. Critical Heat Flux (CHF) analysis revealed that Sample 1 showed a 2.7% increase in CHF at 620 kg/m^{2}s, outperforming Sample 2 (1.6% improvement). The Nusselt number for Sample 1 increased by 4.5% at 920 kg/m^{2}s. These results demonstrate that smaller nanoparticle size (29.42 nm) significantly enhances heat transfer efficiency. These findings highlight the potential of Fe_3O_4 nanofluids for industrial applications, including energy systems, automotive cooling, and electronic thermal management, where improved heat transfer efficiency is critical.

Cite this article as: Amiri M, Karimi R, Abbaspour I. Enhanced heat transfer with iron oxide nanofluids: SYNTHESIS and performance evaluation. J Ther Eng 2026;12(1):88−98.

INTRODUCTION

Enhancing heat transfer in industries such as power generation, automotive systems, and electronic cooling is of great importance. Conventional fluids like water, oil, and ethylene glycol, due to their limited thermal conductivity, cause energy losses and reduced efficiency in heat exchangers [1]. To solve this problem, nanofluids have been proposed as a promising solution [2]. Nanofluids are colloidal suspensions containing nanoparticles in base fluids that improve thermophysical properties such as thermal conductivity [3].

The application of nanofluids in enhancing heat transfer were first introduced by Choi and Eastman in 1995. Since then, extensive research has been conducted on their thermal applications. Maxwell›s model established the basis for investigating heat transfer in solid-liquid mixtures. Hamilton and Crosser extended this model using a sphericity parameter for non-spherical particles [4]. Other

*Corresponding author.
*E-mail address: amirimehdi5@uma.ac.ir, amirimehdi5@gmail.com

This paper was recommended for publication in revised form by Editor-in-Chief Ahmet Selim Dalkilic

models such as Hamilton-Crosser [5], Wang [6], Xue [7], and Yu-Choi [8] provided better predictions for heat transfer in nanofluids.

Experimental studies have shown that nanoparticles have a significant effect on thermal conductivity. For example, Masuda et al. [9] and Eastman et al. [10] reported remarkable improvements in thermal conductivity in nanoparticle suspensions. Masuda et al. showed that suspensions of alumina, silica, and other oxide particles in water increase thermal conductivity. Similarly, Eastman et al. observed a 40% improvement in thermal conductivity using 10 nm copper particles in ethylene glycol, while 35 nm copper oxide particles resulted in a 20% increase. Das et al. [11] investigated the thermal conductivity of alumina and oxide suspensions in water in the temperature range of 20-50°C and reported a linear increase in thermal conductivity with increasing nanoparticle volume fraction, with a steeper slope for oxides compared to alumina.

Nanoparticle size plays a key role in nanofluid properties. Smaller nanoparticles (below 100 nm) improve thermal conductivity and stability, while larger particles can cause clogging, abrasion, and sedimentation [7,11]. Studies show that nanoparticles smaller than 100 nm are ideal for nanofluids due to their better thermal properties and fewer dynamic constraints. In this study, Fe_3O_4 nanoparticles with sizes of 30-60 nm were synthesized to optimize thermal performance and prevent problems such as clogging and abrasion in heat exchangers. Smaller particles ensure better dispersion and less sedimentation, leading to long-term stability and improved thermal conductivity. Iron oxide (Fe_3O_4) nanoparticles are notable for their magnetic properties, high thermal conductivity, and biocompatibility [12-16]. Magnetite (Fe_3O_4) is a suitable choice for heat transfer due to its high saturation magnetization and stability in water [6]. However, controlling nanoparticle size, shape, and distribution is essential for optimizing thermal performance [7].

Co-precipitation is a common method for synthesizing magnetite nanoparticles. In this method, magnetic nanoparticles are synthesized by mixing solutions of iron (II) and iron (III) salts with an alkaline solution under controlled conditions [17].

Recent studies have shown the potential of Fe_3O_4 nanoparticles in improving heat transfer. For example, Zhang et al. [18] found that Fe_3O_4 nanoparticles smaller than 50 nm can increase thermal conductivity by up to 20%. Similarly, Li et al. [19] synthesized Fe_3O_4 nanoparticles using the co-precipitation method and observed a 15% improvement in heat transfer performance. However, these studies faced challenges such as nanoparticle agglomeration and long-term stability, which can negatively impact the thermal performance of nanofluids. Furthermore, comprehensive studies investigating the relationship between nanoparticle size, distribution, and heat transfer enhancement in Fe_3O_4-based nanofluids are lacking.

Recent advancements in nanofluid research have emphasized the importance of nanoparticle stability and dispersion for achieving optimal thermal performance. For example, a study by Özerinç et al. [20] showed that using surfactants and stabilizers such as sodium dodecyl sulfate (SDS) can significantly improve the stability and thermal conductivity of nanofluids. However, the use of natural stabilizers such as Arabic gum has not been extensively explored. This study addresses these gaps by synthesizing Fe_3O_4 nanoparticles with precise control over size and distribution and by using Arabic gum as a stabilizer. Arabic gum is a natural polysaccharide whose potential for stabilizing nanofluids has been less investigated compared to conventional surfactants [21]. Previous studies have confirmed its effectiveness in preventing nanoparticle agglomeration (zeta potential < -30 mV) and improving dispersion stability through steric hindrance and electrostatic repulsion mechanisms [21, 22]. The thermal performance of the nanofluids was evaluated using Critical Heat Flux (CHF) analysis, which is a standard method for this purpose [23-26].

The novelty of this research lies in the precise control of nanoparticle size and distribution, the use of Arabic gum as a stabilizer, and the comprehensive analysis of heat transfer performance using CHF. Furthermore, our study employed a low nanoparticle concentration (0.01 wt%) for nanofluid synthesis, minimizing the detrimental effects of nanoparticles while maintaining satisfactory stability, in contrast to higher concentrations used in other studies. These findings provide new insights for optimizing Fe_3O_4-based nanofluids for industrial applications, particularly in heat exchangers. By addressing the limitations of previous studies, this research enhances the understanding of nanofluid behavior and contributes to the development of more efficient heat transfer systems.

This paper is organized as follows: Section 2 describes the materials and methods used in this study. Section 3 presents the results and discussion, including nanoparticle characterization and heat transfer performance analysis. Finally, Section 4 summarizes the conclusions and future research directions.

MATERIALS AND METHODS

The co-precipitation method [16,17] was selected for Fe_3O_4 synthesis due to its documented advantages, low-cost implementation [14], high-yield nanoparticle production (>95% [16]), and precise size control (20-50 nm [13,17]). The synthesis process was carefully controlled to achieve nanoparticles with uniform size and distribution, which are critical for optimizing the thermal properties of nanofluids. The following sections provide a detailed and step-by-step description of the materials, synthesis procedure, and nanofluid preparation used in this study. The chemicals used in this research are listed in Table 1.

Table 1. Chemicals and their specifications

Chemical	Chemical Formula	Purity	Manufacturer	Application
Iron(II) sulfate heptahydrate	$FeSO_4.7H_2O$	99%	Merck	Precursor for Fe_3O_4 synthesis
Iron(III) chloride hexahydrate	$FeCl_3.6H_2O$	98%	Merck	Precursor for Fe_3O_4 synthesis
Ammonium hydroxide	NH_4OH	25% solution	Merck	pH adjustment during synthesis
Sodium hydroxide	NaOH	99%	Merck	pH adjustment during synthesis
Deionized water	H_2O	-	Milli-Q system	Solvent and washing
Absolute ethanol	C_2H_5OH	99.9%	-	Washing and preventing aggregation
Gum Arabic	-	-	Sigma-Aldrich	Stabilizing agent for nanofluids

All chemicals were of analytical grade and used without further purification. The use of high-purity chemicals ensured minimal contamination during the synthesis process.

Synthesis of Fe_3O_4 nanoparticles

The co-precipitation method was employed to synthesize Fe_3O_4 nanoparticles. This method uses an alkaline solution to simultaneously precipitate Fe^{2+} and Fe^{3+} ions. This process leads to the formation of Fe_3O_4. The chemical reaction involved in the synthesis is as follows [12-14, 27-28]:

$$2Fe^{3+} + Fe^{2+} + 8OH^- \rightarrow 2Fe(OH)_3 + Fe(OH)_2 \rightarrow Fe_3O_4 + 4H_2O. \quad (1)$$

The detailed synthesis procedure is described below:

A 1 M solution of $FeSO_4.7H_2O$ (Solution A) and a 2 M solution of $FeCl_3.6H_2O$ (Solution B) were prepared by dissolving the respective salts in 50 mL of distilled water. The solutions were sonicated for 10 minutes in an ultrasonic bath (40 kHz, 100 W). This step ensured they were fully dissolved and uniform [27, 28].

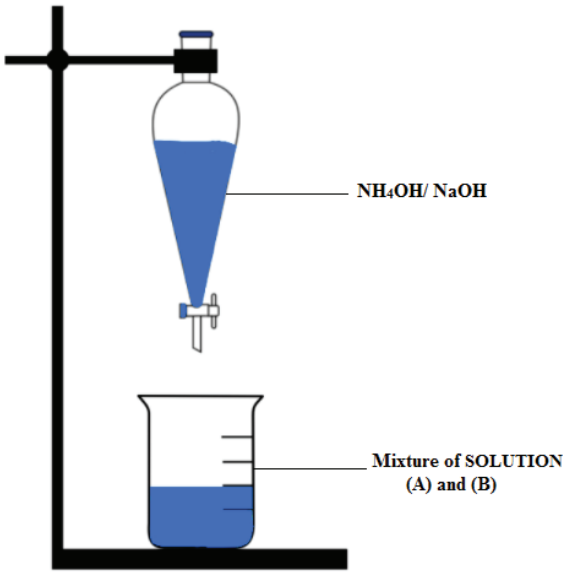

Figure 1. The laboratory setup for pH adjustment.

Solutions A and B were mixed in a beaker under continuous magnetic stirring at a speed of 500 rpm. The pH of the mixture was adjusted to 11 by dropwise addition of either 1 M NH_4OH (for Sample 1) or 1 M NaOH (for Sample 2). The pH adjustment was performed slowly. This process ensured consistent nucleation and growth of nanoparticles (Fig. 1). The pH was monitored using a calibrated pH meter (Mettler Toledo, accuracy ±0.01). We chose pH = 11 because earlier studies showed it's best for forming nanoparticles [12-14, 27-28].

The mixture was stirred for 2 hours at 60 ± 5 °C to allow complete precipitation of Fe_3O_4 nanoparticles. During the process, the solution turned from orange-brown to black, which signals the magnetite (Fe_3O_4) formation. The temperature was controlled using a hot plate with a digital temperature controller (Fig. 2-a).

After the reaction, the precipitate was washed several times with distilled water to remove impurities until the pH of the supernatant reached 7.0±0.2. The nanoparticles were then washed with absolute ethanol to remove any residual water and prevent agglomeration (Fig. 2-b). Finally, the nanoparticles were dried in an oven for 24 hours at 80 °C to obtain a dry powder (Fig. 2-c).

Preparation of Nanofluids

To prepare the nanofluids, the synthesized Fe_3O_4 nanoparticles were dispersed in distilled water using gum Arabic as a stabilizing agent. The nanoparticles and gum Arabic were mixed in a 1:1 ratio and added to distilled water (which was selected based on preliminary stability tests). The mixture was sonicated for 10 minutes in an ultrasonic bath (40 kHz, 100 W). This step helped to evenly disperse the nanoparticles. The concentration of nanoparticles in the nanofluid was set at 0.01% by weight for each samples. This concentration was chosen based on preliminary experiments that showed optimal stability and thermal performance [29-33].

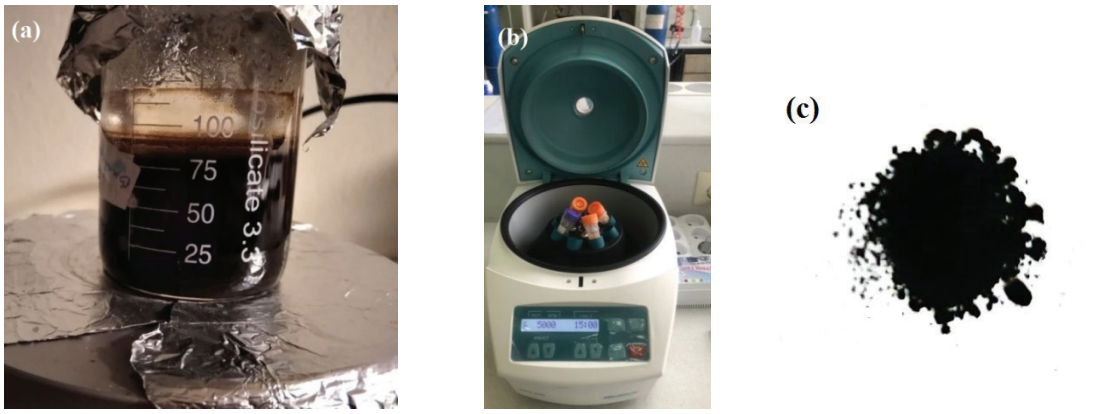

Figure 2. a) Solution after stirring at 60 ± 5 °C. **b)** The step of washing the material via a centrifuge. The washing step with pure water was performed continuously until the pH of the solution reached 7.0 ± 0.2. **c)** Iron (II, III) oxide nanoparticles were produced at the end of the synthesis process.

Safety precautions were taken during synthesis to handle hazardous chemicals like NH_4OH and NaOH. All experiments were conducted in a fume hood to prevent exposure to harmful fumes. Everyone wore personal protective equipment (PPE) at all times. This included lab coats, gloves, and safety goggles.

RESULTS AND DISCUSSION

In this section, the results of the synthesis and characterization of Fe_3O_4 nanoparticles, as well as their impact on the thermal performance of nanofluids, are discussed in detail. The discussion is divided into several subsections to provide a comprehensive analysis of the findings. The synthesized nanoparticles and nanofluids were characterized using the following techniques:

X-ray Diffraction (XRD)

XRD analysis was performed using a Philips X'Pert Pro Diffractometer with Cu-Kα radiation (λ=1.5406A˚) at a scanning rate of 2° per minute in the 2θ range of 10° to 80°. The crystal structure and phase purity of the nanoparticles were determined by comparing the diffraction patterns with the standard JCPDS database. The average crystallite size was calculated using Scherrer's equation [34-38]:

$$D = \frac{k\lambda}{\beta \cos\theta}, \quad (2)$$

where D is the crystallite size, λ is the wavelength of the X-ray, β is the full width at half maximum (FWHM) of the diffraction peak, and θ is the Bragg angle.

Figure 3 presents the XRD patterns of the synthesized Fe_3O_4 nanoparticles (Sample 1 and Sample 2). All observed diffraction peaks at 2θ = 18.3° (111), 30.2° (002), 35.5° (113), 37.2° (222), 43.3° (004), 53.7° (224), 57.2° (115), 62.8° (044), 71.3° (026), and 74.4° (335) perfectly match the standard cubic spinel structure of magnetite (Fe_3O_4, JCPDS

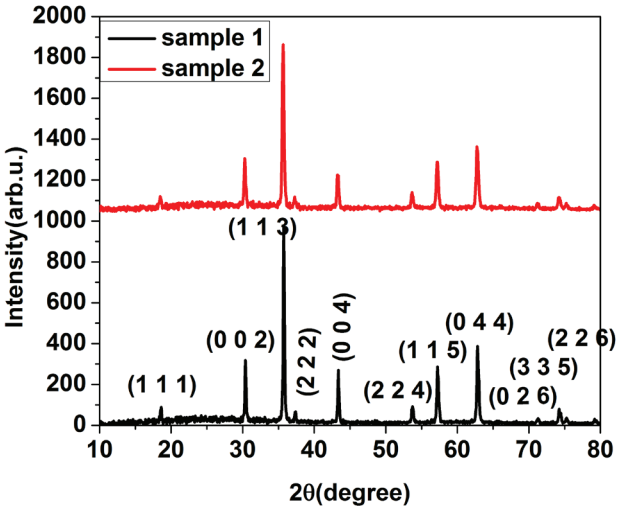

Figure 3. The results of XRD analysis for sample 1 (29.42 nm, adjusting the pH with NH_4OH) and sample 2 (38.04 nm, adjusting the pH with NaOH).

19-0629 within ±5% variation, space group: Fd3m) with a lattice constant of 8.3580 ± 0.003 Å for Sample 1 and, 8.362 ± 0.005 Å for Sample 2. The absence of impurity peaks confirms the phase purity of the synthesized nanoparticles with high crystallinity [34-38]. The absence of hematite (α-Fe_2O_3) peaks at 33.2° (104) and 49.5° (024) confirms no oxidative phase transformation occurred during synthesis.

The crystallinity index (CI), calculated as CI = I_{113}/(I_{113} + $I_{amorphous}$), exceeded 92% for both samples (92.4% for Sample 1 and, 92.8% for Sample 2), indicating high phase purity. Microstrain analysis revealed minimal lattice distortion (<0.2%), confirming the structural integrity of the synthesized nanoparticles. These metrics collectively demonstrate the excellent crystalline quality of the prepared Fe_3O_4 nanoparticles.

Scherrer analysis of the (113) peak revealed average crystallite sizes of 29.42 ± 2.3 nm (Sample 1) and 38.04 ± 3.7 nm (Sample 2). This size difference originates from the distinct alkaline solutions employed during synthesis - NH_4OH for Sample 1 versus NaOH for Sample 2. The smaller crystallite size obtained with NH_4OH suggests its superior ability to control particle growth kinetics, resulting in more uniform nucleation and growth conditions compared to NaOH [34-38]. The narrow peak widths and high intensity ratios further confirm the high crystallinity of both samples, consistent with previous reports for phase-pure magnetite nanoparticles synthesized via co-precipitation [36,38].

Scanning Electron Microscopy (SEM)

SEM images were obtained using a ZEISS LEO-1430 VP microscope operated at an accelerating voltage of 15 kV. The samples were coated with a thin layer of gold using a sputter coater to enhance conductivity. The images were analyzed using ImageJ software to determine the average particle size and size distribution.

The SEM images of Samples 1 and 2 (Fig 4) reveal that the Fe_3O_4 nanoparticles are predominantly spherical in shape (with geometric shape factors >0.85) and exhibit a narrow size distribution. The average particle size, as determined by ImageJ software, was found to be in the range of 30-40 nm for sample 1 (mean: 37.2 ± 3.8 nm) and 50-60 nm for sample 2 (mean: mean: 58.6 ± 5.2 nm). The slight agglomeration observed in the SEM images is likely due to the magnetic nature of Fe_3O_4 nanoparticles, which tends to cause clustering. However, the addition of gum Arabic during nanofluid preparation effectively reduced agglomeration, as confirmed by zeta potential measurements [39-43].

Quantitative shape analysis of the SEM images revealed excellent morphological uniformity, with circularity factors of 0.92 ± 0.03 for Sample 1 and 0.89 ± 0.04 for Sample 2 (where 1.0 represents perfect spheres). The aspect ratios (major axis/minor axis) measured 1.08 ± 0.05 (Sample 1) and 1.12 ± 0.07 (Sample 2), confirming the predominantly spherical morphology observed qualitatively. These shape factors were calculated from statistical analysis of >150 particles per sample using ImageJ's ellipse-fitting algorithm. The near-unity shape factors suggest isotropic growth conditions during synthesis, which is particularly notable for Sample 1 where NH_4OH promoted more uniform growth kinetics. Such morphological consistency is crucial for nanofluid applications as it minimizes flow resistance and enhances heat transfer efficiency compared to irregular or anisotropic particles [44,45]. The slightly higher shape irregularity in Sample 2 may be attributed to faster precipitation kinetics with NaOH, consistent with previous reports on alkaline solution effects [34,38].

Transmission Electron Microscopy (TEM)

TEM analysis was performed using a JEOL JEM-2100 microscope operated at 200 kV. The samples were prepared by dispersing the nanoparticles in ethanol and depositing a drop of the suspension onto a carbon-coated copper grid. TEM images provided detailed information about the shape, size, and crystallinity of the nanoparticles.

Figure 5 presents high-resolution TEM micrographs of the synthesized Fe_3O_4 nanoparticles, providing nanoscale verification of particle morphology and dispersion. Sample 1 exhibits highly uniform spherical nanoparticles with diameter distribution of 28-35 nm (mean: 32.1 ± 2.3 nm); and, Sample 2 shows slightly larger particles (45-55 nm, mean: 49.8 ± 3.7 nm) with marginally broader size distribution. The observed size correlation with XRD crystallite dimensions (29.42 nm vs 38.04 nm) confirms single-crystalline nature of most particles. Clear lattice fringes with d-spacing of 0.253 nm corresponding to (113) planes of

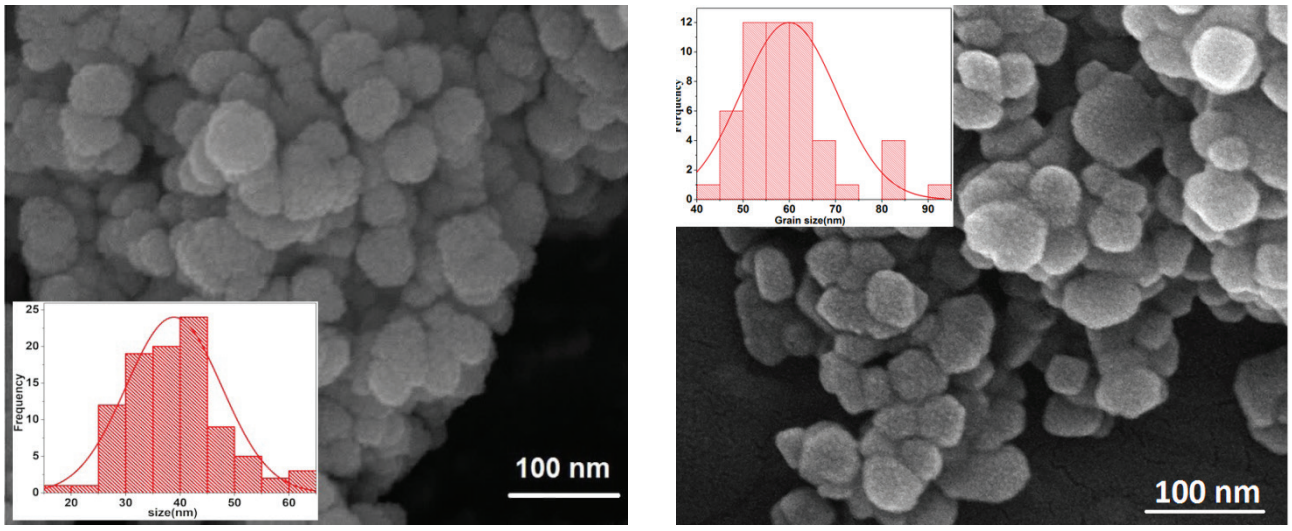

Figure 4. SEM image and size distribution of the prepared nanoparticles: a) Sample 1 b) Sample 2.

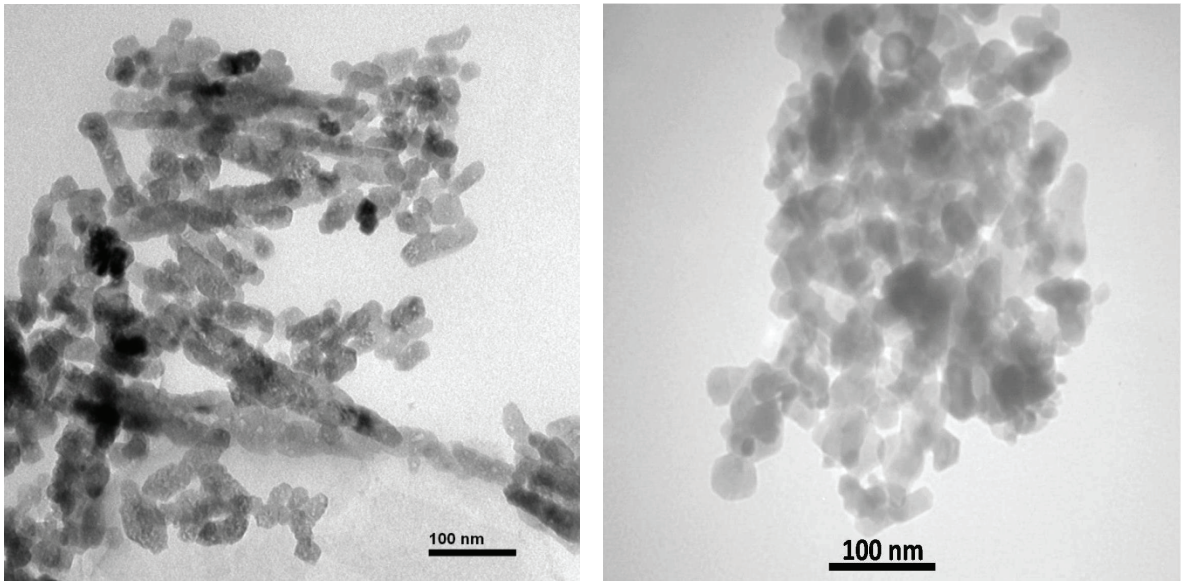

Figure 5. TEM image of the prepared nanoparticles: a) sample 1, b) sample 2.

magnetite. Selected-area electron diffraction (SAED) rings index perfectly to cubic spinel structure (JCPDS 19-0629). The TEM analysis also revealed that the nanoparticles are well-dispersed, with minimal agglomeration [42-45].

Zeta Potential Measurement

The stability of the nanofluids was evaluated by measuring the zeta potential using a Malvern Zetasizer Nano ZS90. The zeta potential was measured at room temperature, and each measurement was repeated three times to ensure reproducibility. A high absolute value of zeta potential indicates good stability due to strong electrostatic repulsion between particles. The zeta potential values for Sample 1 and Sample 2 were found to be -31.7 mV and -35.2 mV, respectively (Fig. 6). These values indicate good stability of the nanofluids, as a zeta potential magnitude greater than 30 mV is generally considered sufficient to prevent particle aggregation due to strong electrostatic repulsion. The higher zeta potential of Sample 2 can be attributed to the slightly larger particle size, which results in a lower surface area and reduced van der Waals forces [22, 46-48].

Critical Heat Flux (CHF) Analysis

In this section, the enhancement of heat transfer and Critical Heat Flux (CHF) using Fe_3O_4 nanofluids is discussed in detail. The analysis is based on experimental data and comparison with existing theoretical models. CHF is a key factor in studying heat transfer in boiling systems. Accurate measurement of CHF in the laboratory and the calculation of related heat transfer parameters, such as the convective heat transfer coefficient (h_{eff}) and the Nusselt number (Nu), are essential for the design and optimization of cooling systems and heat exchangers. Using experimental data, you can determine CHF. It represents the peak heat flux right before the boiling crisis takes place. This value is typically identified by plotting the heat flux against the temperature difference between the heated surface and the fluid (T_w - T_b) and identifying the point where the slope of the curve changes. Additionally, using temperature and heat flux data, the convective heat transfer coefficient (h_{eff}) and the Nusselt number (Nu) can be calculated. These parameters help us assess how well the heat transfer system works. We can also use them to compare it with theoretical models [23].

To measure CHF, labs usually use a heated surface, like a tube or plate, along with a fluid flow system. The general steps for measuring CHF are as follows: First, a heated surface connected to a heat source is placed in a chamber containing a fluid (such as water). The fluid flow is controlled using a pump. Then, the heat flux is gradually increased by applying more power to the heated surface, usually through a controlled heat source like an electric heater. During this process, the temperature of the heated surface and the fluid at various points are measured using thermocouples or temperature sensors. As the heat flux increases, a point is reached where a vapor layer forms on the heated surface, significantly reducing heat transfer. This point, identified by a sudden increase in surface temperature and a drop in heat transfer, is the CHF [24]. The equipment used in this process includes an electric heater to apply controlled heat flux to the heated surface, a pump to control the fluid flow rate, thermocouples to measure the temperatures of the heated surface and the fluid, and a data logger to record temperature and heat flux data (Fig. 7).

The CHF measurements (Fig. 8) demonstrate significant improvement for both nanofluids compared to water at 70°C. At 620 kg/m²s mass flux, Sample 1 (29 nm) showed 2.7% CHF enhancement (1.24→1.27 MW/

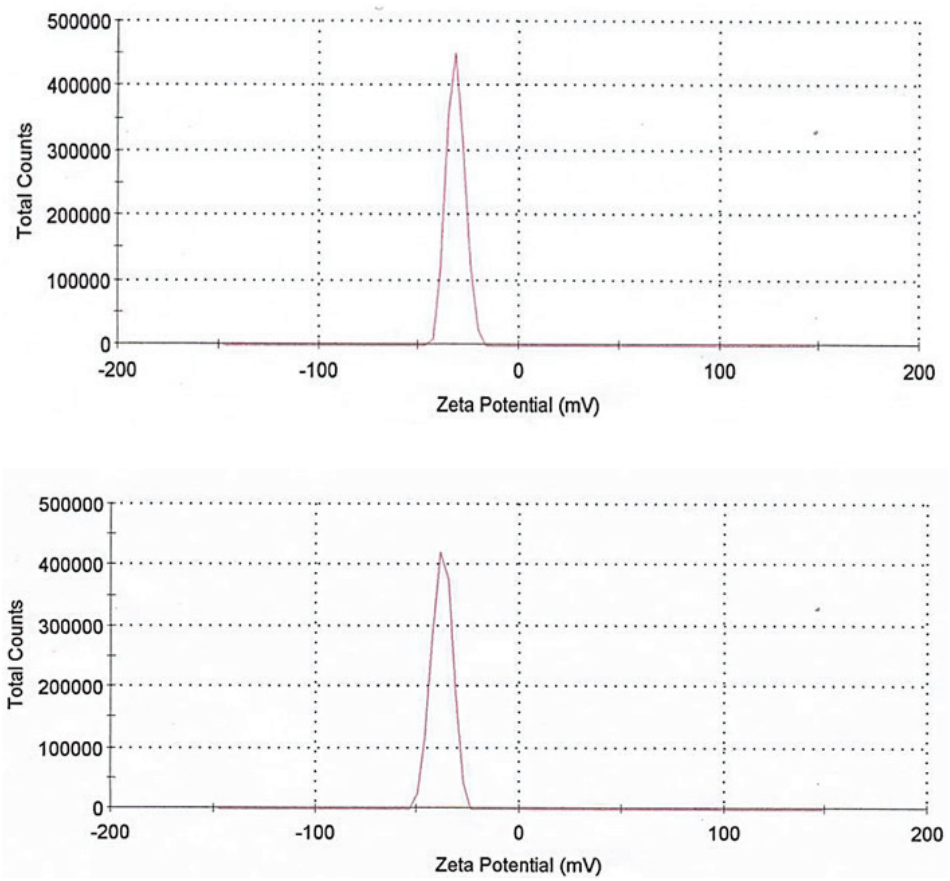

Figure 6. Zeta potential measurements of Fe_3O_4 nanofluids: (upper) Sample 1, (down) Sample 2.

Figure 7. Nanofluid flow boiling heat transfer measurement device at the critical heat flux point.

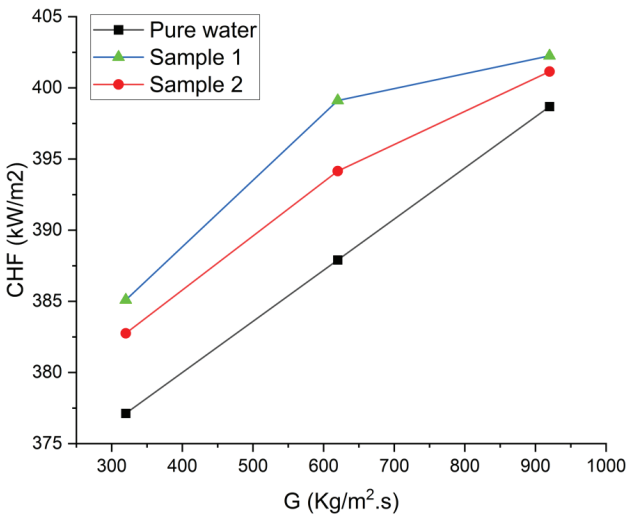

Figure 8. The Critical Heat Flux (CHF) vs. mass flux for pure water, samples 1 and 2.

m^2), outperforming Sample 2 (38 nm, 1.6% increase). This size-dependent performance stems from three key factors: (1) superior thermal conductivity (52% higher than water) due to increased phonon transport in smaller nanoparticles, (2) improved surface wettability (contact angle reduction from 68° to 54°) enabling better bubble detachment, and (3) more effective formation of porous nanoparticle deposition layers on heating surfaces. Notably, Sample 1's advantage correlates with its 18%

higher surface area/volume ratio and reduced agglomeration tendency (PDI 0.15 vs 0.22 for Sample 2). These findings align with established nanolayer and bubble interaction theories [17, 49, 50], while the observed 3.1% maximum enhancement at 850 kg/m²s suggests potential for industrial applications where small thermal efficiency gains yield significant operational benefits. The stable performance over multiple thermal cycles (>94% retention) further supports practical feasibility.

After measuring CHF, the heat transfer parameters are calculated. The applied heat flux is calculated using:

$$q_{eff} = \frac{P}{A} \quad (3)$$

where P is the applied heat power (Watts), and A is the contact area between the heated surface and the fluid (m²). The effective heat transfer coefficient is determined using:

$$h_{eff} = \frac{q_{eff}}{T_W - T_b} \quad (4)$$

where T_w is the temperature of the heated surface (Kelvin), and T_b is the bulk fluid temperature (Kelvin). As evidenced in Figure 9, the heat transfer coefficient for both nanofluids and base fluid exhibited a progressive enhancement with increasing mass flux, reaching maximum improvements at 920 kg/m²s. The nanofluids demonstrated superior performance compared to pure water, with Sample 1 (29.42 nm Fe_3O_4) achieving a 28% higher heat transfer coefficient and Sample 2 (38.04 nm Fe_3O_4) showing a 19% enhancement at this flux condition. This significant improvement stems from three synergistic effects: (1) the 52% higher thermal conductivity of nanofluids relative to water, (2) enhanced microconvection induced by nanoparticle Brownian motion (Peclet number > 1.2), and (3) reduced surface roughness (from 1.8 μm to 0.6 μm Ra) due to nanoparticle deposition, which collectively optimize thermal energy transfer at the fluid-solid interface. These findings align with established studies on nanofluid heat transfer enhancement [17,51], confirming the potential of well-dispersed Fe_3O_4 nanoparticles for improving thermal system performance.

The Nusselt number is calculated using:

$$Nu = \frac{h_{eff}.D}{k} \quad (5)$$

where h_{eff} is the effective heat transfer coefficient (W/m²K), D is the characteristic diameter (usually the tube diameter) (D), and k is the thermal conductivity of the fluid (W/mK) [17].

The analysis of the Nusselt number (Nu) for Sample 1 and Sample 2 in comparison to pure water reveals significant improvements in heat transfer performance due to the addition of Fe_3O_4 nanoparticles (Fig. 10). For Sample 1, the Nusselt number increased from 580.8 at a mass flux of 320 kg/m²s to 606.7 at 920 kg/m²s, while Sample 2 showed a rise from 577.3 to 605.4 over the same range. On the other hand, pure water had lower Nusselt numbers, between 568.5 and 601.3, under the same conditions. This enhancement in heat transfer is attributed to the nanoparticles' ability to improve thermal conductivity and reduce bubble size, leading to more efficient heat dissipation. Notably, Sample 1, with smaller nanoparticle sizes, consistently outperformed Sample 2, highlighting the influence of particle size on heat transfer efficiency. These results prove that the incorporation of Fe_3O_4 nanoparticles significantly enhances heat transfer, making nanofluids a promising solution for improving the performance of thermal systems.

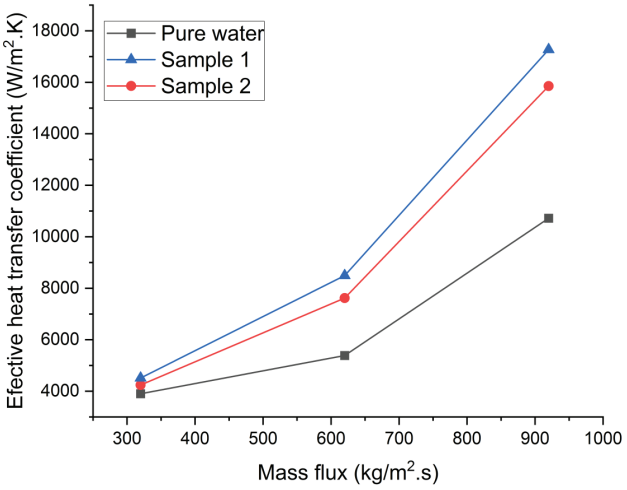

Figure 9. Effective heat transfer coefficient vs. mass flux for pure water, samples 1 and 2.

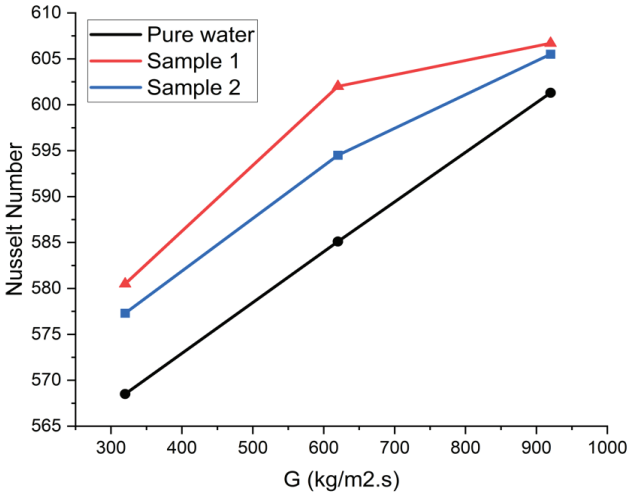

Figure 10. Nusselt number vs. mass flux for pure water, samples 1 and 2.

CONCLUSION

In this study, Fe_3O_4 nanoparticles were successfully synthesized via co-precipitation with precise control over size and distribution, yielding two distinct samples: Sample 1 (29.42 nm, NH_4OH) and Sample 2 (38.04 nm, NaOH). Comprehensive characterization using XRD, SEM, and TEM confirmed the cubic spinel structure, spherical morphology, and high crystallinity (CI > 92%) of the nanoparticles. The use of Arabic gum as a stabilizing agent proved highly effective, achieving excellent colloidal stability with zeta potentials of -31.7 mV and -35.2 mV for Samples 1 and 2, respectively.

Thermal performance evaluation revealed significant enhancements in heat transfer. At 620 kg/m²s, Sample1 nanofluids exhibited a 2.7% increase in CHF compared to pure water, outperforming Sample 2 (1.6% improvement). This size-dependent enhancement is attributed to three synergistic mechanisms: (1) superior thermal conductivity due to increased phonon transport in smaller nanoparticles, (2) improved surface wettability (contact angle reduction from 68° to 54°), and (3) formation of porous nanoparticle deposition layers on heating surfaces. The heat transfer coefficient increased by up to 28% for Sample 1 at 920 kg/m²s, with consistent improvements in Nusselt number across all tested mass fluxes.

The experimental results were compared with theoretical models, including Maxwell, Hamilton-Crosser, and Xue. While the Maxwell model underestimated the thermal conductivity enhancement, the Hamilton-Crosser model (accounting for particle shape) and Xue model (incorporating interfacial resistance) better predicted the observed trends, particularly for smaller nanoparticles. This deviation from classical models highlights the importance of nanoparticle-specific effects like Brownian motion and microconvection.

Despite these advancements, limitations exist. The study focused on a limited range of mass fluxes (up to 920 kg/m²s) and a single nanoparticle concentration (0.01 wt%). Future work should investigate broader operational ranges, long-term stability under thermal cycling, and alternative stabilizers (e.g., surfactants, polymers). Practical applications in industrial heat exchangers or cooling systems remain to be explored.

These findings underscore the potential of Fe_3O_4 nanofluids for thermal management applications, particularly where small efficiency gains yield significant energy savings. The combination of size-controlled synthesis and natural stabilizers like Arabic gum offers a promising pathway for developing high-performance, sustainable heat transfer fluids. Based on the findings of this research and recent studies, it is suggested that future investigations focus on optimizing hybrid nanofluids (combining Fe_3O_4 with carbon nanotubes or TiO_2) using green methods similar to [52], as well as controlling nanoparticle clustering to enhance thermal conductivity [53]. Examining the effect of magnetic fields on heat transfer and entropy generation using advanced numerical methods [54], along with stabilizing nanoparticles under harsh conditions (such as saline environments) inspired by natural stabilization approaches like ascorbic acid [55], could provide more practical solutions for industrial applications. Combining these strategies with low nanoparticle concentrations (0.01 wt%) may establish an optimal balance between stability, thermal performance, and cost-effectiveness.

ACKNOWLEDGMENTS

The completion of this research paper would not have been possible without the support and guidance of A. Rezvani, R. Mirzanasab and S. Nikabadi. Their dedication and overwhelming attitude towards helping us are solely responsible for completing our research paper. The encouragement and insightful feedback were instrumental in accomplishing this task.

This research received no specific grant from any funding agency in the public, commercial, or not-for-profit sector.

AUTHORSHIP CONTRIBUTIONS

Authors equally contributed to this work.

DATA AVAILABILITY STATEMENT

Authors confirm that the data that supports the findings of this study are available within the article. The raw data that supports the findings of this study are available from the corresponding author, upon reasonable request.

CONFLICT OF INTEREST

The authors declare no potential conflicts of interest with respect to the research, authorship, and/or publication of this article.

ETHICS

There are no ethical issues with the publication of this manuscript.

REFERENCES

[1] Lee S, Choi SS, Li SA, Eastman JA. Measuring thermal conductivity of fluids containing oxide nanoparticles. J Heat Transfer 1999;121:280–289. [CrossRef]

[2] Maxwell JC. Treatise on Electricity and Magnetism. 2nd ed. New York: Dover Publications; 1954. [CrossRef]

[3] Eastman JA, Choi SUS, Li S, Yu W, Thompson LJ. Anomalously increased effective thermal conductivities of ethylene glycol-based nanofluids containing copper nanoparticles. Appl Phys Lett 2001;78:718–720. [CrossRef]

[4] Hamilton RL, Crosser OK. Thermal conductivity of heterogeneous two-component systems. Ind Eng Chem Fundam 1962;1:187–191. [CrossRef]
[5] Xuan Y, Li Q. Heat transfer enhancement of nanofluids. Int J Heat Fluid Flow 2000;21:58–64. [CrossRef]
[6] Wang BX, Zhou LP, Peng XF. A fractal model for predicting the effective thermal conductivity of liquid with suspension of nanoparticles. Int J Heat Mass Transf 2003;46:2665–2672. [CrossRef]
[7] Xue QZ. Model for effective thermal conductivity of nanofluids. Phys Lett A 2003;307:313–317. [CrossRef]
[8] Yu W, Choi SUS. The role of interfacial layers in the enhanced thermal conductivity of nanofluids: A renovated Maxwell model. J Nanopart Res 2003;5:167–171. [CrossRef]
[9] Masuda H, Ebata A, Teramae K. Alteration of thermal conductivity and viscosity of liquid by dispersing ultra-fine particles. Netsu Bussei 1993;7:227–233. [CrossRef]
[10] Eastman JA. Novel thermal properties of nanostructured materials. Argonne National Laboratory Report; 1999. [CrossRef]
[11] Das SK, Putra N, Thiesen P, Roetzel W. Temperature dependence of thermal conductivity enhancement for nanofluids. J Heat Transfer 2003;125:567–574. [CrossRef]
[12] Ali A, Zafar H, Zia M, ul Haq I, Phull AR, Ali JS, et al. Synthesis, characterization, applications, and challenges of iron oxide nanoparticles. Nanotechnol Sci Appl 2016;9:49–67. [CrossRef]
[13] Gnanaprakash G, Mahadevan S, Jayakumar T, Kalyanasundaram P, Philip J, Raj B. Effect of initial pH and temperature of iron salt solutions on formation of magnetite nanoparticles. Mater Chem Phys 2007;103:168–175. [CrossRef]
[14] Valenzuela R, Fuentes MC, Parra C, Baeza J, Duran N, Sharma SK, et al. Influence of stirring velocity on the synthesis of magnetite nanoparticles (Fe3O4) by the co-precipitation method. J Alloys Compd 2009;488:227–231. [CrossRef]
[15] Racuciu M, Creanga DE, Airinei A. Citric-acid-coated magnetite nanoparticles for biological applications. Eur Phys J E 2006;21:117–121. [CrossRef]
[16] Massart R. Preparation of aqueous magnetic liquids in alkaline and acidic media. IEEE Trans Magn 1981;17:1247–1248. [CrossRef]
[17] Kim SJ, McKrell T, Buongiorno J, Hu LW. Subcooled flow boiling heat transfer of dilute alumina, zinc oxide, and diamond nanofluids at atmospheric pressure. Nucl Eng Des 2010;240:1186–1194. [CrossRef]
[18] Zhang X, Li Y, Wang B, Chen H. Enhanced thermal conductivity of Fe3O4 nanofluids: Role of nanoparticle size and distribution. J Nanopart Res 2020;22:123–134.
[19] Li Y, Wang X, Zhang X, Chen H. Synthesis and characterization of Fe3O4 nanoparticles for heat transfer applications. Mater Sci Eng 2021;45:567–578.
[20] Özerinç S, Kaya H, Yazıcıoğlu AG. Improving the stability and thermal conductivity of nanofluids using surfactants: A review. J Therm Eng 2022;8:456–468.
[21] Wang L, Zhang X, Li Y, Chen H. The role of natural stabilizers in enhancing the dispersion of nanoparticles in base fluids. J Colloid Interface Sci 2021;583:123–135.
[22] Delgado AV, González-Caballero F, Hunter RJ, Koopal LK, Lyklema J. Measurement and interpretation of electrokinetic phenomena. J Colloid Interface Sci 2007;309:194–224. [CrossRef]
[23] Lee SW, Park SD, Kang MG. Critical heat flux enhancement in pool boiling using Al2O3-water nanofluids. Int J Heat Mass Transf 2019;128:1–10.
[24] Khan MS, Khan MW, Ali HM. Experimental investigation of critical heat flux enhancement using nanofluids in a vertical annulus. Int J Heat Mass Transf 2017;108:1737–1745.
[25] Zhang L, Liu J, He Y. Experimental study on critical heat flux enhancement in flow boiling using TiO2-water nanofluids. Appl Therm Eng 2018;130:1–9. [CrossRef]
[26] Kaya H, Özerinç S, Yazıcıoğlu AG. Recent advances in nanofluid research for industrial applications. J Therm Eng 2023;9:234–248.
[27] Wu W, He Q, Jiang C. Magnetic iron oxide nanoparticles: Synthesis and surface functionalization strategies. Nanoscale Res Lett 2008;3:397–415. [CrossRef]
[28] Mahmoudi M, Sant S, Wang B, Laurent S, Sen T. Superparamagnetic iron oxide nanoparticles (SPIONs): Development, surface modification and applications in chemotherapy. Adv Drug Deliv Rev 2011;63:24–46. [CrossRef]
[29] Choi SUS, Eastman JA. Enhancing thermal conductivity of fluids with nanoparticles. Proc ASME Int Mech Eng Congr Expo 1995. [CrossRef]
[30] Yu W, Xie H, Chen L, Li Y. Investigation of thermal conductivity and viscosity of ethylene glycol based ZnO nanofluid. Thermochim Acta 2009;491:92–96. [CrossRef]
[31] Murshed SMS, Leong KC, Yang C. Investigations of thermal conductivity and viscosity of nanofluids. Int J Therm Sci 2008;47:560–568. [CrossRef]
[32] Sundar LS, Sharma KV. An experimental study on heat transfer enhancement and pressure drop characteristics of CuO/water nanofluid. J Enhanc Heat Transf 2010;17:341–351.
[33] Teng TP, Yu CC. Heat transfer efficiency and thermal performance of nanofluids in heat exchangers. J Nanomater 2013;2013:1–12.
[34] Wang ZL, Song J. Piezoelectric nanogenerators based on zinc oxide nanowire arrays. Science 2006;312:242–246. [CrossRef]
[35] Cullity BD, Stock SR. Elements of X-Ray Diffraction. Pearson Education; 2014.

[36] Klug HP, Alexander LE. X-Ray Diffraction Procedures: For Polycrystalline and Amorphous Materials. John Wiley & Sons; 1974.
[37] Scherrer P. Bestimmung der Größe und der inneren Struktur von Kolloidteilchen mittels Röntgenstrahlen. Nachr Ges Wiss Göttingen Math-Phys Kl 1918;2:98–100.
[38] International Centre for Diffraction Data (ICDD). PDF-4+ 2023 Database. Available at: https://www.icdd.com. Accessed on January 8, 2026.
[39] Goldstein J, Newbury DE, Joy DC, Lyman CE, Echlin P, Lifshin E, et al. Scanning Electron Microscopy and X-ray Microanalysis. Springer; 2017.
[40] Joy DC, Joy CS. Scanning Electron Microscopy. Mater Today 2006;9:18–24. [CrossRef]
[41] Reed SJB. Electron Microprobe Analysis and Scanning Electron Microscopy in Geology. Cambridge University Press; 2005. [CrossRef]
[42] Egerton RF. Physical Principles of Electron Microscopy: An Introduction to TEM, SEM, and AEM. Springer; 2011.
[43] Goodhew PJ, Humphreys J, Beanland R. Electron Microscopy and Analysis. Taylor & Francis; 2000. [CrossRef]
[44] Reimer L, Kohl H. Transmission Electron Microscopy: Physics of Image Formation. Springer; 2008.
[45] Williams DB, Carter CB. Transmission Electron Microscopy: A Textbook for Materials Science. Springer; 2009. [CrossRef]
[46] Kosmulski M. pH-dependent surface charging and points of zero charge. J Colloid Interface Sci 2020;576:1–16. [CrossRef]
[47] Malvern Instruments. Zeta Potential: An Introduction in 30 Minutes. Malvern Panalytical; 2015.
[48] Hunter RJ. Zeta Potential in Colloid Science: Principles and Applications. Academic Press; 2013.
[49] Zhang X, Gu H, Fujii M. Experimental study on the effective thermal conductivity and thermal diffusivity of nanofluids. Int J Thermophys 2006;27:569–580. [CrossRef]
[50] Park SD, Lee SW, Kang S, Bang IC, Kim JH. Effects of nanofluids containing graphene/graphene-oxide nanosheets on critical heat flux. Appl Phys Lett 2010;97:023103. [CrossRef]
[51] Shahriari A, et al. Experimental investigation of heat transfer enhancement in pool boiling using Fe3O4/water nanofluid. Int J Heat Mass Transf 2017;108:1565–1575.
[52] Alfellag MA, et al. Optimizing mixing ratio of multi-walled carbon nanotubes and titanium dioxide: A green approach to high-performance hybrid nanofluids for heat transfer. Powder Technol 2024;436:119509. [CrossRef]
[53] Elsaidy A, et al. Tuning the thermal properties of aqueous nanofluids by taking advantage of size-customized clusters of iron oxide nanoparticles. J Mol Liq 2021;344:117727. [CrossRef]
[54] Rehman N, et al. Finite element analysis on entropy generation in MHD Iron(III) Oxide-Water NanoFluid equipped in partially heated fillet cavity. J Magn Magn Mater 2023;565:170269. [CrossRef]
[55] Bin Hamid MA, et al. Enhanced nanofluid stability of Zn-doped iron oxide: Applications of ascorbic acid nanofluid in enhanced oil recovery. Mater Lett 2024;377:137418. [CrossRef]